Computational Materials Science 135 (2017) 64–77

Contents lists available at ScienceDirect

Computational Materials Science

journal homepage: www.elsevier.com/locate/commatsci

A multiscale model for amorphous materials

Shingo Urata [a,b], Shaofan Li [b,*]

[a] Innovative Technology Research Center, Asahi Glass Co., Ltd., 1150 Hazawa-cho, Kanagawa-ku, Yokohama, Kanagawa 221-8755, Japan
[b] Department of Civil and Environmental Engineering, University of California, Berkeley, CA 94720, USA

ARTICLE INFO

Article history:
Received 9 October 2016
Received in revised form 20 March 2017
Accepted 22 March 2017
Available online 17 April 2017

Keywords:
Amorphous materials
Cauchy-Born rule
Fracture
Multiscale cohesive zone model
Multiscale simulation

ABSTRACT

In this work, we proposed a Cauchy-Born rule (CBR) based multiscale model to study mechanical properties of amorphous materials. In this work, we combine a coarse-grained Parrinello-Rahman (CG-PR) method and the Multiscale Cohesive Zone Model (MCZM) method to model the Lennard-Jones (L-J) binary glass and amorphous silicon (a-Si) solid. The proposed CG-PR method applies the CBR to a representative volume element of an amorphous material with representative microstructure pattern, whose side dimension is about twice of the cutoff distance of interatomic interaction. Numerical simulations were carried out, and it is found that CG-RP method can reproduce the stress-strain relations extrapolated from large scale MD simulations for both L-J binary glass as well as amorphous silicon (a-Si).

The CG-PR method is then combined with MCZM method to simulate failure process of amorphous materials. We found that (1) the CG-PR method can capture the history-dependent inelastic stress-strain relation in amorphous materials, and (2) the CG-PR enhanced MCZM method can simulate both brittle and ductile fracture in both a-Si solid and L-J binary glass. Moreover, the multiscale methodology developed here may be extended to study mechanical properties of a variety of other non-crystalline materials.

1. Introduction

The Cauchy-Born rule (CBR) is basically a kinematic assumption on atoms motions in crystalline materials. Utilizing the CBR assumption, one can develop multiscale methods to construct macroscale constitutive models for crystalline materials, which are informed by atomic or molecular information at microscale. Historically, Cauchy assumed that the macroscale deformation motion and the atomistic movement in multiplying scale factor. This concept was further extended by Born who introduced macroscopic deformation gradient as a linear transformation of position vectors in the reference configuration to describe atom arrangements [1]. By assuming that both kinematic motions in macroscale and microscale are affine deformation, many multiscale models have been developed to establish constitutive models for various crystalline solids by utilizing with interatomic interaction potentials, e.g. [2–4] among others.

In specific, because that the Cauchy-Born rule assumes uniform deformation in crystalline solids, we can estimate atom positions $\mathbf{r}$ in deformed configuration simply as $\mathbf{r}_i = \mathbf{F} \cdot \mathbf{R}_i$, where $\mathbf{F}$ is the deformation gradient, and $\mathbf{R}_i$ is referential coordinate of atom. For example, the local form of the quasi-continuum (QC) method [2,5] uses the interpolation field among the representative atoms to describe a continuous atomistic displacement field, which provides an estimate for each atom's displacement in the domain. Multiscale Cohesive Zone Model (MCZM) [4,6] applies the same technique to a MD unit cell consisting of multiple atoms, which is assigned to each quadrature point inside an (finite) element. Since the unit cell is embedded in each quadrature point of a finite element, we can use it to evaluate both constitutive relation as well as the cohesive law at that material point. This procedure provides great advantage to evaluate stress-strain relation for crystalline solids, especially for single crystals. This is because that in each element one only needs to calculate stress at the locations of a few quadrature points. As a result of such simplification, computational cost is greatly reduced to simulate material behaviors at macroscale based on microscale information. For example, as the Bravais lattice, both face-centered (FCC) and body-centered cubic (BCC) crystals have only one atom in their Wigner-Seitz cells. When evaluating stress at one quadrature point, one only needs to calculate atomistic interaction around that atom, which are only involved with a few dozen neighboring atoms. For non-Bravie lattices, for example the cubic diamond crystal, its lattice structure may be considered as a pair of interpenetrating FCC lattices, thus it is also

* Corresponding author at: Department of Civil and Environmental Engineering, University of California, Berkeley, CA 94720, USA.
E-mail address: shaofan@berkeley.edu (S. Li).

http://dx.doi.org/10.1016/j.commatsci.2017.03.029
0927-0256/

possible to apply CBR by adding additional degree of freedom that represents the distance between two atoms inside its Wigner-Seitz cell [6,7].

Based on this technique, a number of multiscale methods have been developed for crystalline materials whose lattices resemble the diamond crystal lattice such as silicon or other semiconductor crystals e.g. [2,8,9]. On the other hand, the Cauchy Born rule has been extended to include nonlinear deformation by considering the contribution of higher order deformation gradients. For examples, Sunyk and Steinmann have applied the higher order Cauchy-Born rule in crystalline solids with inhomogeneous deformation by considering the second order deformation [10]. CBR has also been applied to membrane sheets of graphenes, thin plates of mutilayer graphenes, and nanowires by introducing the so-called exponential CBR that takes into account the curvature effect in deformation mapping [11,12]. In order to distinguish bulk crystal and crystal surface region, Park et al. proposed the concept of the surface CBR [13], and they also applied the method to study surface effect on silicon [14]. Khoei et al. further extended the idea to take in account of corner and edge effects on microscale silicon [15]. Li et al. have applied up to fourth order CBR to describe different types of crystal defects to study dislocation dynamics [16].

Contrary to single crystal materials, studies of multiscale modeling for amorphous materials are relatively limited, despite of the fact that there exist a large variety of amorphous materials, such as glasses, ceramics, amorphous semiconductors and various polymer materials, in engineering applications. This is largely due to the complexity and difficulty in amorphous material modeling [17]. Most of amorphous material modelings are restricted at the mesoscale level by using the homogenization methodology in micromechanics [18], for example, using the approach of Eshelby's equivalent inclusion method [19], which assumes a homogeneous material with equivalent eigenstrains corresponding to heterogeneous material. For instance, Liu and Sun employed the method to estimate effective elastic stiffness and yield strength of amorphous nanocomposites [20].

However, recently, Albaret et al. attempted to connect micromechanics approach with molecular dynamics approach by combining the Eshelby inclusion method with molecular dynamics (MD) simulations to study amorphous silicon material [21]. Valavala et al. also tried to predict hyperelastic continuum constitutive relation for Polyimide and Polycarbonate based on MD simulations [22]. Other efforts have been made for multiscale modeling of amorphous polymers. The Pseudo-Amorphous Cell (PAC) method employs representative volume elements (RVE) to model amorphous materials, in which atom displacements are related to the cell deformation without assuming continuous displacement field by using so-called transformation matrix operator for small deformation regions [23–25]. The RVE approach in micromechanics is also applied to amorphous polymetric material by coupling molecular dynamics calculations with the finite element calculations [26]. Almost of all these studies adopt micromechanics homogenization scheme to build a hierarchical modeling, but no CBR technique has ever been involved. To the best of the authors' knowledge, the research on using CBR to non-crystal materials is exiguous [17,27].

It is fair to say that so far there have been no systematic studies on how to apply CBR based multiscale methods to model amorphous materials, in terms of extrapolating macroscale constitutive relations based on atomistic information. Even though CBR may be a limited approach to model amorphous materials, it might be still useful to utilize its simplicity and low-cost to model amorphous materials. Therefore in this study we hope to examine the possibility as well as limitation on how to use CBR modeling amorphous materials, and compare it with other multiscale methods and the molecular dynamics approach. In particular, based on CBR, we have developed a coarse-grained Parrinello-Rahman (CG-PR) method that is tailored for dealing with complex microstructure of amorphous materials. In this work, we shall mainly focus on how to use the proposed CB-PR method and the multiscale cohesive zone method to model amorphous silicon (a-Si) and Lennard-Jones (L-J) binary glass. This is because that these two models are not only simple enough for the fundamental study, but also are representatives for amorphous materials. Moreover, a-Si is a typical brittle material with prototypical amorphous structure though it may be characterized as a monoatomic material. Furthermore, a-Si is a material that has a great potential for solar cell [28], thin-film transistor [29], flexible display, and many other applications. On the other hand, L-J binary glass is an ideal model for glassy materials with ductility, such as metallic glasses [30,31] and polymer network glasses [32].

The paper is organized in five sections. The simulation methods of MD, coarse-grained Parrinello-Rahman (CG-PR) and MCZM are described in Section 2. Numerical examples are presented in Section 3, in which we compare the simulation results between MD and CG-PR/MCZM for both a-Si solid and L-J binary glass. By analyzing the simulation results, we hope to find a general guideline for application of CBR to amorphous materials. After these examinations, we combined CG-PR method with multiscale cohesive zone model to simulate fracture of amorphous materials, and the simulation results are reported in Section 4. Finally in Section 5, we conclude the study with a few remarks.

2. Simulation methods

In this section, we shall briefly discuss the simulation methodologies that are used in this study, which include: molecular dynamics (MD), the Cauchy-Born based coarse-grained Parrinello-Rahman (CG-PR) method, and the multiscale cohesive zone model (MCZM).

2.1. Molecular dynamics simulation

All MD simulations were carried out by using LAMMPS [33]. Amorphous silicon (a-Si) is modeled by using three body Tersoff potential [34,35] that can be expressed as follows,

$$V_{ij}^{TS} = f_C(r_{ij})[f_R(r_{ij}) + b_{ij} f_A(r_{ij})]. \tag{1}$$

In the Tersoff potential, the functions f_R, f_A are defined as,

$$f_R(r_{ij}) = A\exp(-\lambda_{ij} r_{ij}); \tag{2}$$

$$f_A(r_{ij}) = -B\exp(-\mu_{ij} r_{ij}), \tag{3}$$

and the cutoff function f_C is defined as,

$$f_C(r_{ij}) = \begin{cases} 1 & r_{ij} \leqslant R_{ij} \\ \frac{1}{2} + \frac{1}{2}\cos\left(\frac{\pi(r_{ij}-R_{ij})}{S_{ij}-R_{ij}}\right) & R_{ij} < r_{ij} < S_{ij} \\ 0 & r_{ij} \geqslant S_{ij} \end{cases}. \tag{4}$$

In order to take into account the three body interaction, the Tersoff potential has a parameter b_{ij} (see Eq. (1)). It explicitly depends on the location of the third atom k, which is expressed as follows,

$$b_{ij} = (1 + \beta^n \zeta_{ij}^n)^{\frac{-1}{2n}} \tag{5}$$

$$\zeta_{ij} = \sum_{k \neq i,j} f_c(r_{ik}) g(\theta_{ijk}) \tag{6}$$

$$g(\theta_{ijk}) = 1 + \frac{c^2}{d^2} - \frac{c^2}{d^2 + (h - \cos\theta_{ijk})^2}. \tag{7}$$

For more information on the parameters of the Tersoff potential, readers may consult [35]. In the rest of the paper, we may refer the amorphous silicon as a-Si solid.

We used the Lennard-Jones (L-J) potential to model the binary glass, and the L-J potential can be expressed as follows,

$$V^{LJ} = 4\varepsilon_{ij}\left\{\left(\frac{\sigma_{ij}}{r_{ij}}\right)^{12} - \left(\frac{\sigma_{ij}}{r_{ij}}\right)^{6}\right\}. \quad (8)$$

In the rest of the paper, we may refer it as L-J binary glass.

The binary system is composed of two different sizes of particles, A and B, at the ratio of 80:20. In the multiscale modeling and simulation, the parameters of the binary system are chosen from the well studied parameter sets in the literature e.g. [31,32,36]. In specific, we choose the following key parameters in the simulation: for the energy depths, $\varepsilon_{AA} = 1.0\varepsilon_0$, $\varepsilon_{BB} = 1.5\varepsilon_0$, and $\varepsilon_{AB} = 0.5\varepsilon_0$; for the particle size parameters, $\sigma_{AA} = 1.0\sigma_0, \sigma_{BB} = 0.8\sigma_0$ and $\sigma_{AB} = 0.88\sigma_0$, respectively. The potential is truncated at $2.245\sigma_0 A$. In order to connect the binary system with real materials, we assume that the particle A is silicon (see [37]), which means that ε_0 and σ_0 are 2.4503 [kJ/mol] and 3.385 [Å], respectively.

Initial configurations for both stretch and shear simulations were prepared by first quenching the a-Si system from melted state at high temperature; and we followed the procedure suggested in [38], in which the effect of quenching rate has been studied in details. The recommended quench rate is less than 10^{12} [K/s] in order to avoid inappropriate structural defects. In this study, we firstly melted crystal silicon at 3500 [K] by using the canonical ensemble MD (NVT). After equilibrating at 3500 [K], the system was quenched to 300 [K] at quench rate 10^{12} [K/s]. In other words, it took 3.2 [ns] to cool the system from 3500 [K] to 300 [K]. The system was then equilibrated at 300 [K] by using isothermal-isobaric ensemble (NPT) with stress free, and finally it is relaxed by using conjugate gradient (CG) method [39] to eliminate residual stress. Time interval of all simulations for silicon was 0.1 [fs], and temperature was controlled with by the Nosé-Hoover thermostat [40].

In the numerical simulation, the binary glass system modeled by L-J potential was initially configured in a dilute gas state to avoid particle overlap, and then the system was compressed by applying high pressure. Following the equilibration at normalized temperature ($\overline{T} = 1.0$), the system was quenched until $\overline{T} = 0.02$ with quenching rate 1.96×10^{-4} in normalized L-J unit. After a NPT simulation at $\overline{T} = 0.02$ with stress free condition, the system was eventually optimized by using CG method. Time interval for L-J binary glass was 1.0×10^{-3} in L-J time unit.

2.2. A coarse-grained Parrinello-Rahman (CG-PR) method

In this section, we shall introduce a coarse-grained Parrinello-Rahman (CG-PR) method, and use it to simulate mechanical responses of amorphous materials under the uniaxial and shear deformations under different strain rates in order to evaluate stress-strain relations. To validate the proposed method, we shall compare the CG-PR simulation results with that of molecular dynamics.

In the multiscale finite element method for crystalline lattice materials, the Cauchy-Born rule is applied to a unit cell of a crystal, which is usually "embedded" in a quadrature point within an element, and we can utilize this procedure to obtain macroscale stress at that quadrature point. For amorphous materials, there is no periodically distributed unit cells. In the proposed CG-PR method, we employ a CBR procedure in applied in a representative cell (r-cell) to extrapolate the stress-strain relation. For the L-J binary glass, we prepared three r-cells with different sizes, which include 256, 1000 and 30,000 atoms, respectively. In the simulations of a-Si solid, four different r-cells composed of 64, 216, 1000 and 32,768 atoms each were examined. The minimum size of the simulation system is selected to satisfy a criteria that the box size is larger than twice of the cutoff length of the interatomic interaction.

Since the amorphous material has no definite microstructure, we cannot directly apply CBR to derive its macroscale constitutive relation. In order to develop a viable CBR procedure in amorphous materials, we have developed the following coarse-grained Parrinello-Rahman method, which originates from the well-known Parrinello-Rahman molecular dynamics [41,42].

We first select an r-cell of the amorphous material by identifying its basic mesoscale structure and configuration as shown in Fig. 1. The r-cell selected in multiscale simulation is the same unit cell in the MD simulation, which has the same dimension with the initial configurations generated for MD simulations. We may define a r-cell shape tensor as

$$\mathbf{h}(0) = [\mathbf{a}, \mathbf{b}, \mathbf{c}], \quad (9)$$

where $\mathbf{a}, \mathbf{b}, \mathbf{c}$ are three edge vectors of the unit cell at initial time, as suggested by Parrinello and Rahman [41]. In order to capture the characteristics of amorphous materials, we choose the side length of the minimum r-cell, i.e. $|\mathbf{a}|, |\mathbf{b}|$, and $|\mathbf{c}|$, about twice of the cutoff distance of interatomic potential. Following [41], we may use the cell shape tensor $\mathbf{h}$ to re-scales the initial positions of atoms, i.e.

$$\mathbf{R}_i = \mathbf{h}(0)\mathbf{S}_i, \quad i = 1, 2, \ldots, N_c, \quad (10)$$

where $\mathbf{S}_i$ is the scaled atom positions (see [42] for discussions).

Considering the deformation mapping $\boldsymbol{\varphi} : \mathbf{R} \to \mathbf{r}$, one can define the deformation gradient as

$$\mathbf{F} = \frac{\partial \boldsymbol{\varphi}}{\partial \mathbf{R}}.$$

Apply the Cauchy-Born rule to approximate the deformation mapping $\boldsymbol{\varphi}$, we can use the Cauchy-Born rule to write

$$\mathbf{r}_i = \mathbf{F}\mathbf{R}_i = \mathbf{F} \cdot \mathbf{h}(0) \cdot \mathbf{S}_i = \mathbf{h}(t)\mathbf{S}_i, \quad (11)$$

where $\mathbf{h}(t) = \mathbf{F} \cdot \mathbf{h}(0)$ as shown in Fig. 2.

In PR-MD [41], one solves the motion of $\mathbf{S}_i(t)$ (or $\mathbf{R}_i(t)$) for each atom i, as well as the evolution of cell shape $\mathbf{h}(t)$ (or $\mathbf{F}(t)$) for each unit cell, by using the following equations,

$$\ddot{\mathbf{R}}_i = -\sum_{j \neq i}\left(\frac{V'(r_{ij})}{m_i r_{ij}}\right)(\mathbf{R}_i - \mathbf{R}_j) - \mathbf{C}^{-1} \cdot \dot{\mathbf{C}} \cdot \dot{\mathbf{R}}_i \quad (12)$$

$$W\ddot{\mathbf{F}} = -\Omega_0 \mathbf{F}(\boldsymbol{\mathcal{S}}_{virial} - \boldsymbol{\mathcal{S}}_{ext}), \quad (13)$$

where $\boldsymbol{\mathcal{S}}_{ext}$ is the prescribed external second Piola-Kirchhoff stress; Ω_0 is the volume of MD cell in the referential configuration, and

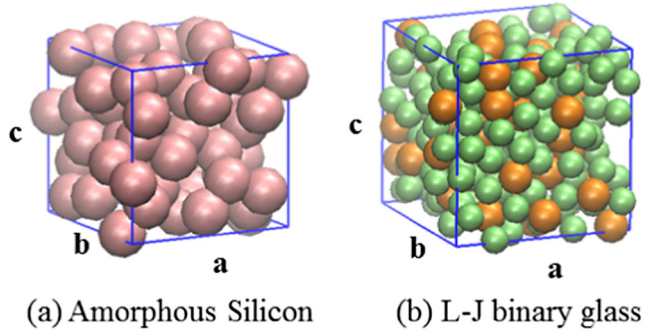

Fig. 1. Examples of the representative cell (r-cell) for amorphous materials: (a) Amorphous Si: 64 atoms, and (b) 80/20 L-J binary glass: 250 atoms. The r-cell shape tensor is defined as: ($\mathbf{h}(0) = [\mathbf{a}, \mathbf{b}, \mathbf{c}]$).

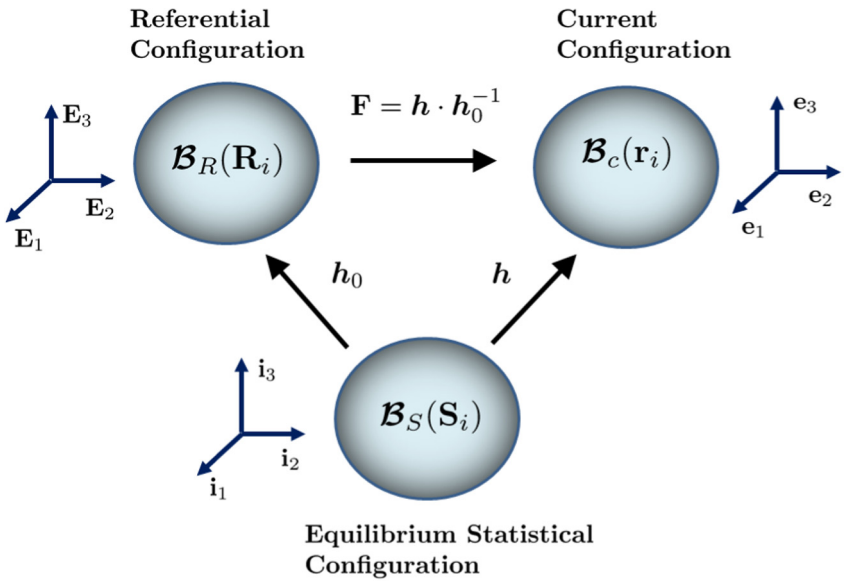

Fig. 2. Illustration of kinematic mapping of the coarse gained Parinnello-Rahman (CG-PR) method.

$$\mathcal{S}_{virial} = \frac{1}{\Omega_0}\sum_i \left(-m_i \dot{\mathbf{R}}_i \otimes \dot{\mathbf{R}}_i + \sum_{j\neg=i} \frac{V'(r_{ij})}{r_{ij}} (\mathbf{R}_j - \mathbf{R}_i) \otimes (\mathbf{R}_j - \mathbf{R}_i) \right)$$
$$= \frac{1}{\Omega_0} \mathbf{h}_0 \cdot \sum_i \left(-m_i \dot{\mathbf{S}}_i \otimes \dot{\mathbf{S}}_i + \sum_{j\neg=i} \frac{V'(r_{ij})}{r_{ij}} (\mathbf{S}_j - \mathbf{S}_i) \otimes (\mathbf{S}_j - \mathbf{S}_i) \right) \cdot \mathbf{h}_0^T, \tag{14}$$

where $V(r_{ij})$ is the atomistic potential of the amorphous solid, and $r_{ij} = |\mathbf{r}_j - \mathbf{r}_i|$. For the detailed discussions and applications of the latest PR-MD, readers may consult [42–44].

In the coarse grained PR method (CG-PR), we do not solve each $\mathbf{S}_i$ explicitly. On the other hand, we use multiscale finite element method to solve $\mathbf{F}(t_n)$ for each element at time $t_n = n\Delta t$. In CG-PR computations, the atom configurations ($\mathbf{r}_{gi}(t_n)$) in the current time step N is guessed from previous configuration by using the Cauchy-Born Rule (CBR),

$$\mathbf{r}_{gi}(t_n) = \mathbf{F}(t_n) \cdot \mathbf{R}_i(t_{n-1}) = \mathbf{F}(t_n) \cdot \mathbf{h}(0) \cdot \mathbf{S}_i(t_{n-1}), \tag{15}$$

where, $\mathbf{h}(0)$ is the initial r-cell shape tensor, $\mathbf{R}_i(t_{n-1})$ is atom coordinate in referential configuration at time step $n-1$, and $\mathbf{S}_i(t_{n-1})$ is normalized coordinates of atoms in the r-cell. Once we have initial guess of coordinate as $\mathbf{r}_{gi}(t_n)$, the configuration is optimized to minimize energy by using CG-PR method with periodic boundary condition in all direction.

$$\mathbf{r}_{opti}(t_n) = \arg\min V(\mathbf{r}_i), \tag{16}$$

with the starting configuration $\mathbf{r}_{gi}(t_n)$.

Inversely, we can find that

$$\mathbf{S}_i(t_n) = (\mathbf{F}(t_n) \cdot \mathbf{h}(0))^{-1} \cdot \mathbf{r}_{opti}(t_n). \tag{17}$$

Similar optimization algorithms have been reported in literature, e.g. [39].

By using the optimized configuration $\mathbf{r}_{opt}(t_n)$, we can calculate the first Piola-Kirchhoff stress tensor $\mathbf{P}$ as follows,

$$\mathbf{P} = \frac{1}{2\Omega_0}\sum_{i\in N}\left(\frac{\partial V}{\partial \mathbf{F}}\right) = \frac{1}{2\Omega_0}\sum_{i\in N}\left(\frac{\partial V}{\partial \mathbf{r}_i}\frac{\partial \mathbf{r}_i}{\partial \mathbf{F}}\right)\Big|_{\mathbf{r}_i=\mathbf{r}_{opti}}, \tag{18}$$

where N is the number of atoms in a r-cell, and Ω_0 is the initial volume of the r-cell. For simplicity, in the rest of the paper, we drop the dependence on $\mathbf{r}_{opti}$.

For the Tersoff potential, we have

$$\mathbf{P}^{TS} = \frac{1}{2\Omega_0}\sum_{i\neq j}^{N}\left(\frac{\partial V_{ij}^{TS}}{\partial \mathbf{F}}\right)$$
$$= \frac{1}{2\Omega_0}\sum_{i\neq j}^{N}\left[\frac{\partial V_{ij}^{TS}}{\partial r_{ij}}\frac{\partial r_{ij}}{\partial \mathbf{F}} + \sum_{k\neq i,k\neq j}^{N}\left(\frac{\partial V_{ij}^{TS}}{\partial r_{ik}}\frac{\partial r_{ik}}{\partial \mathbf{F}} + \frac{\partial V_{ij}^{TS}}{\partial \cos\theta_{ijk}}\frac{\partial \cos\theta_{ijk}}{\partial \mathbf{F}}\right)\right]. \tag{19}$$

While for the L-J potential, we have

$$\mathbf{P}^{LJ} = \frac{1}{2\Omega_0}\sum_{i\neq j}^{N}\frac{\partial V_{ij}^{LJ}}{\partial r_{ij}}\frac{\partial \mathbf{r}_{ij}}{\partial \mathbf{F}}. \tag{20}$$

In above two equations, the following relations are used,

$$\frac{\partial r_{ij}}{\partial \mathbf{F}} = \frac{\partial r_{ij}}{\partial \mathbf{r}_{ij}}\frac{\partial \mathbf{r}_{ij}}{\partial \mathbf{F}} = \frac{\mathbf{r}_{ij}\otimes\mathbf{R}_{ij}}{r_{ij}}, \tag{21}$$

$$\frac{\partial \cos\theta_{ijk}}{\partial \mathbf{F}} = \left(\frac{1}{r_{ik}} - \frac{\cos\theta_{ijk}}{r_{ij}}\right)\frac{\partial r_{ij}}{\partial \mathbf{F}} + \left(\frac{1}{r_{ij}} - \frac{\cos\theta_{ijk}}{r_{ik}}\right)\frac{\partial r_{ik}}{\partial \mathbf{F}} - \left(\frac{r_{jk}}{r_{ij}r_{ik}}\right)\frac{\partial r_{jk}}{\partial \mathbf{F}}. \tag{22}$$

In passing we note that in literature, some defined the macroscale first Piola-Kirchhoff stress as (e.g. [42])

$$\mathbf{P} = \frac{1}{2\Omega_0}\sum_{i\in N_c}\left(\frac{\partial V}{\partial \mathbf{h}}\right) = \frac{1}{2\Omega_0}\sum_{i\in N_c}\left(\frac{\partial V}{\partial \mathbf{F}}\right)\mathbf{h}_0^{-1},$$

because of the Cauchy-Born rule of the tensorial quantity: $\mathbf{h}(t) = \mathbf{F}(t)\cdot\mathbf{h}(0)$.

2.3. Multiscale cohesive zone model

The above CG-PR method provides a CBR procedure to extrapolate macroscale constitutive relations from atomistic information, provided that certain assumptions or approximations are granted.

To carry out macroscale continuum-level simulations, such as failure analysis of a structure made by amorphous material, we often employ multiscale finite element method to compute macroscale deformation of structures and materials, and many

of them are based on CBR procedures. There are several CBR-based multiscale finite element methods e.g. the internal virtual bond model [3], the local quasi-continuum model [39], and the multiscale cohesive zone model [4]. However, in most of these methods, the CBR is specified for crystalline materials.

In this work, we apply the CBR procedure developed in CG-PR method to the Multiscale Cohesive Zone Model (MCZM) [4] to study fracture of amorphous materials. In MCZM, there are two types of elements: bulk elements and cohesive elements. MCZM is also a CBR-based multiscale method combined with cohesive zone model (CZM) concept that has been developed to capture fracture phenomena by inserting fracture process zone between so-called bulk elements [45,46]. However, instead of having zero thickness cohesive zone elements, MCZM adopts finite thin element, namely cohesive zone element, between bulk elements to represent the process zone as shown in Fig. 3.

In MCZM, the bulk element is modeled by the first order Cauchy-Born rule, while the cohesive zone element may be modeled by: (1) The higher order Cauchy-Born rule e.g. [16,47,6]; (2) The first order Cauchy-Born rule with depletion potential [4,48–50], or (3) The first order Cauchy-Born model with bubble mode plus a biased sigmoidal function. In this work, we shall adopt the third approach. The more details can be presented in the following, and to be found in our previous work [6].

To formulate the computational algorithm, we first define total Lagrangian of the continuum system as,

$$\mathcal{L} = \mathcal{K} - (\mathcal{W}_{int} + \mathcal{W}_{ext}), \tag{23}$$

where $\mathcal{W}_{ext}, \mathcal{W}_{int}$ and $\mathcal{K}$ are the external potential energy, the strain energy of the continuum and total kinetic energy, respectively. In Eq. (23),

$$\mathcal{K} = \int_\Omega \frac{1}{2}\rho\dot{\mathbf{u}}\cdot\dot{\mathbf{u}}dV \tag{24}$$

$$\mathcal{W}_{int} = \int_\Omega W(\mathbf{F})dV, \tag{25}$$

where W is the strain energy density functional of strain, ρ and $\dot{\mathbf{u}}$ are the mass density and velocity field of the continuum, respectively.

The Hamiltonian principle can then be derived in terms of displacement variation,

$$\int_{t_0}^{t_1} (\delta\mathcal{K} - (\delta\mathcal{W}_{int} + \delta\mathcal{W}_{ext}))dt = 0, \tag{26}$$

where

$$\int_{t_1}^{t_2} \delta\mathcal{K}dt = \int_{t_1}^{t_2}\int_\Omega \rho\dot{\mathbf{u}}\cdot\delta\dot{\mathbf{u}}dVdt = -\int_{t_1}^{t_2}\int_\Omega \rho\ddot{\mathbf{u}}\cdot\delta\mathbf{u}dV\,dt, \tag{27}$$

$$\delta\mathcal{W}_{int} = \int_\Omega \left[\frac{\partial W}{\partial \mathbf{F}} : \delta\mathbf{F}\right]dV = \int_\Omega [\mathbf{P} : \delta\mathbf{F}]dV, \tag{28}$$

$$\delta\mathcal{W}_{ext} = -\int_\Omega \mathbf{b}\cdot\delta\mathbf{u}dV - \int_{\delta\Omega_t} \bar{\mathbf{T}}\cdot\delta\mathbf{u}dS. \tag{29}$$

In Eq. (29), $\mathbf{b}$ is the body force inside the bulk medium, and $\bar{\mathbf{T}}$ is the traction vector on the surface $\delta\Omega_t$, respectively. Consequently, the Galerkin weak formulation can be formulated in terms of element summation as follows,

$$\begin{aligned}
&\mathop{\mathbf{A}}_{e=1}^{n_B^e}\left\{\int_{\Omega_B^e}\left(\rho_0\ddot{\mathbf{u}}^h\cdot\delta\mathbf{u} + \mathbf{P} : \delta\mathbf{F}^h\right)dV\right\} + \mathop{\mathbf{A}}_{e=1}^{n_C^e}\left\{\int_{\Omega_C^e}\mathbf{P} : \delta\mathbf{F}^h dV\right\} \\
&= \mathop{\mathbf{A}}_{e=1}^{n_B^e}\left\{\int_{\Omega_B^e}\rho_0\mathbf{b}\cdot\delta\mathbf{u}^h dV\right\} + \mathop{\mathbf{A}}_{e=1}^{n_C^e}\left\{\int_{\Omega_C^e}\rho_0\mathbf{b}\cdot\delta\mathbf{u}^h dV\right\} \\
&\quad + \mathop{\mathbf{A}}_{e=1}^{n_B^e}\left\{\int_{\Gamma_t}\bar{\mathbf{T}}\cdot\delta\mathbf{u}^h dS\right\},
\end{aligned} \tag{30}$$

where, Ω_B^e is the domain of bulk element e; Ω_C^e is the domain of CZ element e; Γ_t is the traction boundary of the system; and n_B^e and n_C^e are number of bulk and CZ elements, respectively. The superscript h used in the above equation is the standard notation in computational mechanics to represent a discretized displacement field corresponding to FEM interpolation field.

Because specimens are discretized by using tetrahedral bulk elements, CZ element is constructed as a triangular-shaped prism element (wedge element) as seen in Fig. 3. In our recent work, we have found that a bubble node additionally inserted to CZ element can capture inhomogeneous deformation, which is related to the inherent weakness of CZ, even if higher order CBR is not employed [6]. Therefore, we adopt seven nodes wedge element to CZ elements. The additional bubble node locates on the center of wedge element, and its position in ζ direction is reflected to the deformation gradient $\mathbf{F}$ by using a sigmoidal function.

$$\zeta_{bub}(t) = \frac{2}{1+\exp\{-P_{nl}(|\mathbf{F}(t-1)\cdot\mathcal{N}|-1)\}} - 1, \tag{31}$$

where, $\mathcal{N}$ is the normal vector of the CZ element and $\mathbf{F}(t-1)$ is the first order deformation gradient at previous time step, and thus $|\mathbf{F}\cdot\mathcal{N}|$ represents degree of deformation in the direction of cohesive zone element thickness. According to the normalized coordinate of the bubble node, it is possible to calculate displacement vector $\mathbf{d}_{bub}$ of the bubble node, with assuming $\xi_{bub}, \eta_{bub} = 1/3$.

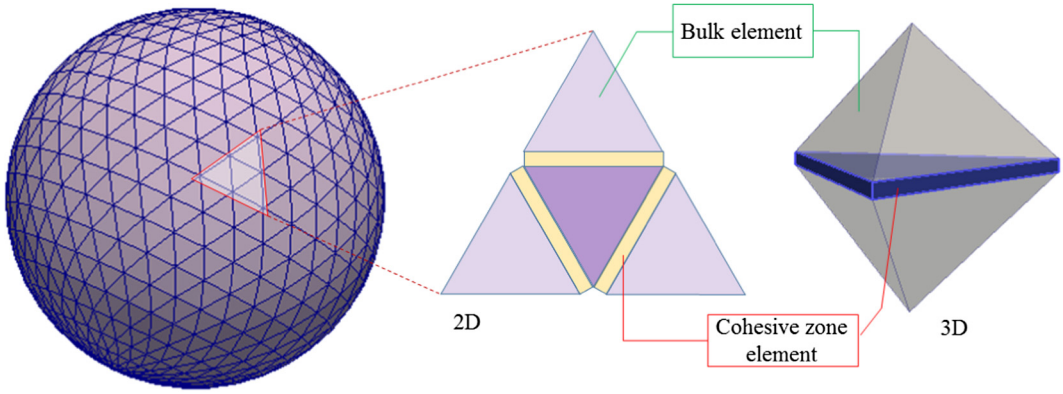

Fig. 3. Illustration of the concept and mesh discretization of multiscale cohesive zone model (MCZM).

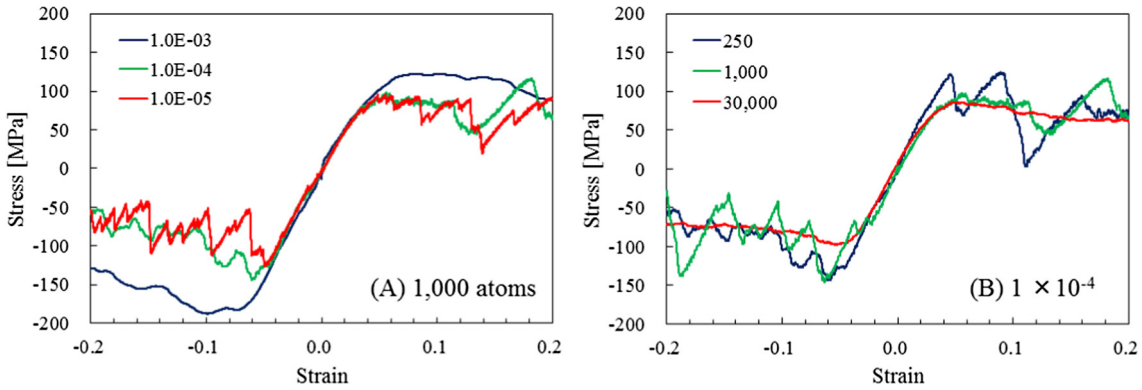

Fig. 4. Uniaxial stress-strain relation of Lennard-Jones binary glass obtained from MD simulation: (A) 1000 atoms system at $\dot{\varepsilon} = 1.0 \times 10^{-5}$ to 1.0×10^{-3}. (B) 250, 1000 and 30,000 atoms systems with $\dot{\varepsilon} = 1.0 \times 10^{-4}$.

Table 1
Mechanical properties of Lennard-Jones binary glass estimated by MD simulations.

No. of atom	Strain rate ($\dot{\varepsilon}$) shear strain rate ($\dot{\gamma}$)	σ_{33}^{max} [MPa]	σ_{33}^{min} [MPa]	E_y [GPa]	σ_{13}^{max} [MPa]	G [GPa]
250	1.0×10^{-4}	125	−146	3.06	97	1.28
	1.0×10^{-3}	122	−187	2.12	88	1.05
1000	1.0×10^{-4}	98	−144	2.46	79	1.09
	1.0×10^{-5}	96	−126	2.49	76	1.30
30,000	1.0×10^{-4}	86	−98	2.03	42	0.93

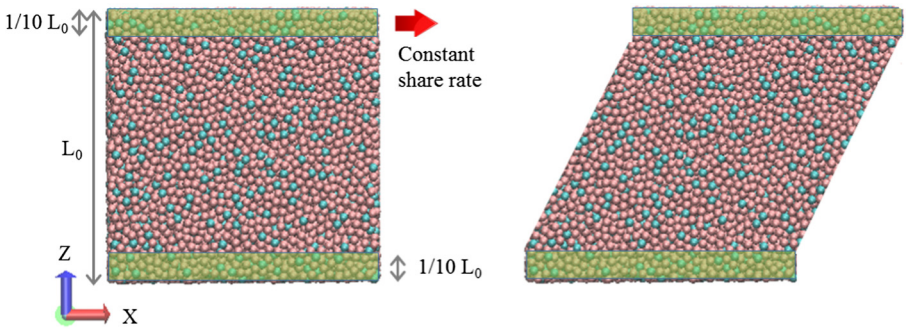

Fig. 5. Schematic illustration of boundary condition of shear simulation. Freedom of atoms within 10% range from top and bottom is frozen. The group of top region is moved toward X direction, while the bottom region is fixed at the initial position. Periodic boundary conditions are assumed in X and Y directions but not in Z direction.

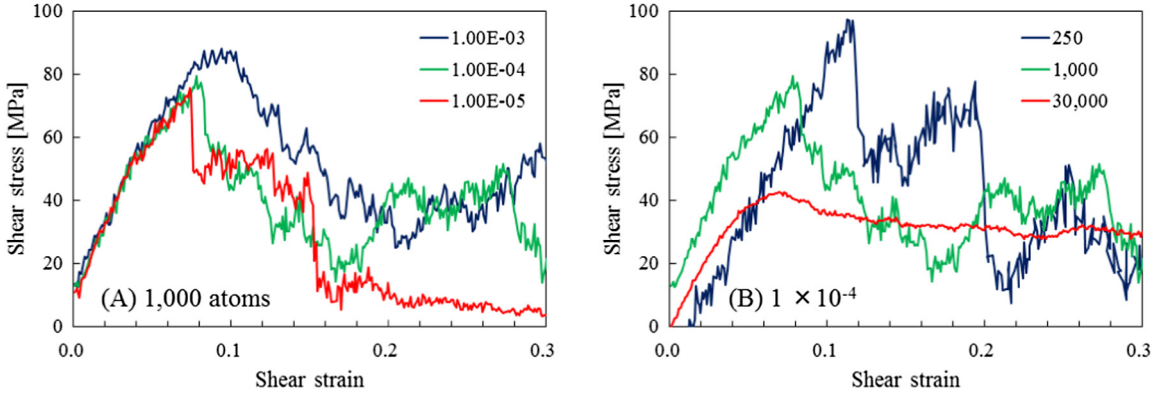

Fig. 6. MD simulation results of shear stress-strain relation of Lennard-Jones binary glass. (A) 1000 atoms system at $\dot{\gamma} = 1.0^{-5}$ to 1.0^{-3}. (B) 250, 1000 and 30,000 atoms systems at $\dot{\gamma} = 1.0^{-4}$.

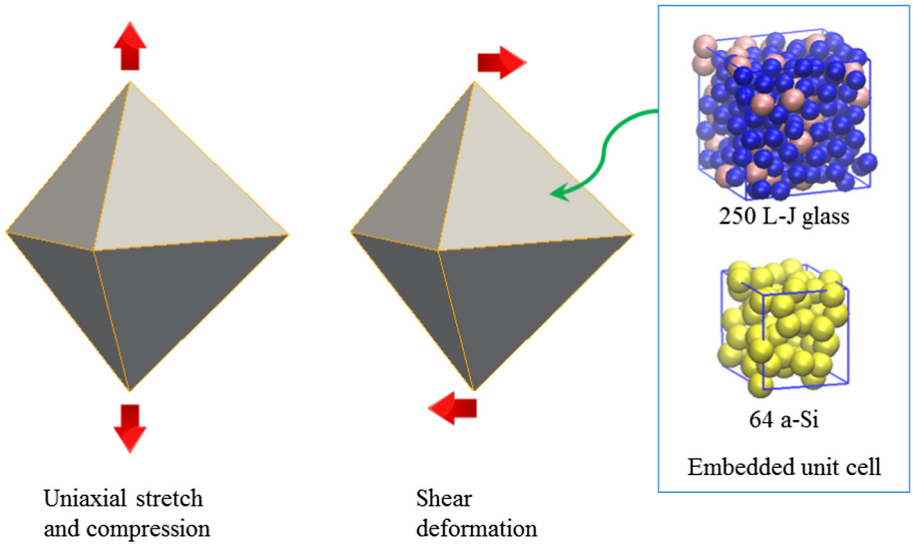

Fig. 7. Simple benchmark tests for CG-PR method based finite element model, in which polyatomic r-cells are embedded in each element.

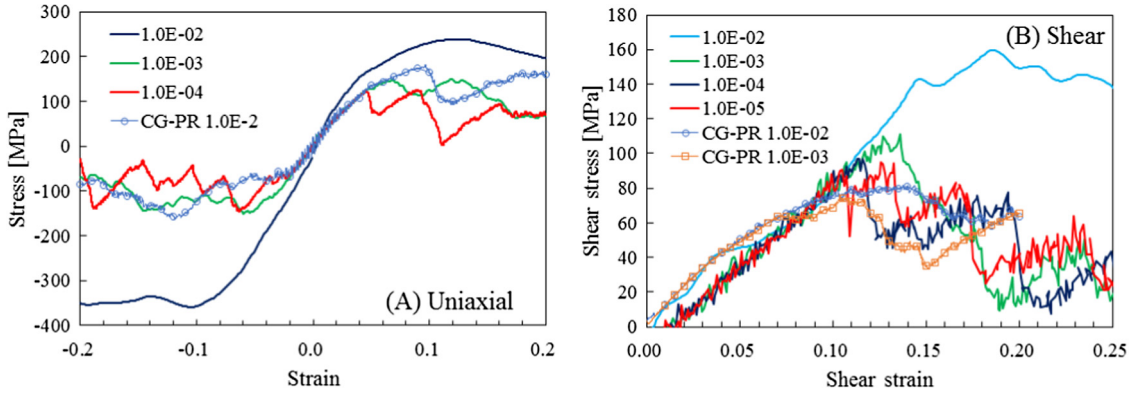

Fig. 8. Comparison of CG-PR method for L-J binary glass with simple two element model (Fig. 7) and MD simulations. (A) Uniaxial stretch and compression, (B) Shear deformation. 250 atoms r-cell is examined. Deformation rates are shown in legend.

$$\mathbf{d}_{bub} = \sum_{i=1}^{6} N_i\left(\xi = \frac{1}{3}, \eta = \frac{1}{3}, \zeta = \zeta_{bub}(t)\right)\mathbf{d}_i. \tag{32}$$

The shape function matrix **N** and a procedure to define bubble function and bubble node position can be found in [6].

Using FEM interpolation functions, we can approximate the displacement field as follows,

$$\mathbf{u}^h(\mathbf{X}) = \sum_{i=1}^{n_{node}} \mathbf{N}_i(\mathbf{X})\mathbf{d}_i, \tag{33}$$

where n_{node} is number of node in an element. According to Eqs. (30) and (33), the discrete equations of motion for FEM node displacements can be derived as,

$$\mathbf{M}\ddot{\mathbf{d}} + \mathbf{f}^{int}(\mathbf{d}) - \mathbf{f}^{cohe}(\mathbf{d}) = \mathbf{f}^{ext}, \tag{34}$$

where, **M** is the mass matrix, and $\mathbf{f}^{int}$, $\mathbf{f}^{cohe}$ and $\mathbf{f}^{ext}$ are force vectors from bulk elements, CZ elements and external force, respectively. These quantities are defined as follows,

$$\mathbf{M} = \mathop{\mathbf{A}}_{e=1}^{n_B^e} \int_{\Omega_B^e} \rho_0 \mathbf{N}^{eT}\mathbf{N}^e dV \tag{35}$$

$$\mathbf{f}^{int} = \mathop{\mathbf{A}}_{e=1}^{n_B^e} \int_{\Omega_B^e} \mathbf{B}^{eT}\mathbf{P}^e(\mathbf{d}) dV \tag{36}$$

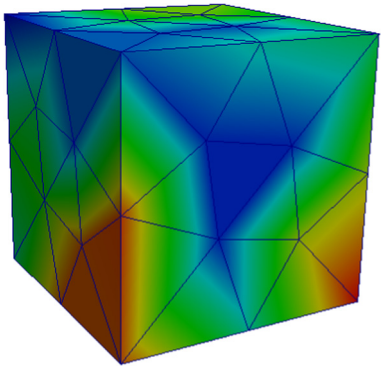

Fig. 9. Cubic specimen composed of 100 bulk elements. Color shows stress distribution of Cauchy stress in *Z* direction generated by random orientation of the r-cell in each element. (For interpretation of the references to colour in this figure legend, the reader is referred to the web version of this article.)

$$\mathbf{f}^{ext} = \mathop{\mathbf{A}}_{e=1}^{n_B^e} \left\{ \int_{\Omega_B^e} \mathbf{N}^{eT}\mathbf{B}^e dV + \int_{\partial\Gamma_t} \mathbf{N}^{eT}\bar{\mathbf{T}}^e dS \right\} \tag{37}$$

$$\mathbf{f}^{cohe} = \mathop{\mathbf{A}}_{e=1}^{n_{elem}^{CZ}} \int \mathbf{B}^{eT}\mathbf{P}^e(\mathbf{d}) dV, \tag{38}$$

where, ρ_0 is material density, $\mathbf{B}^e$ is the element strain-displacement matrix,

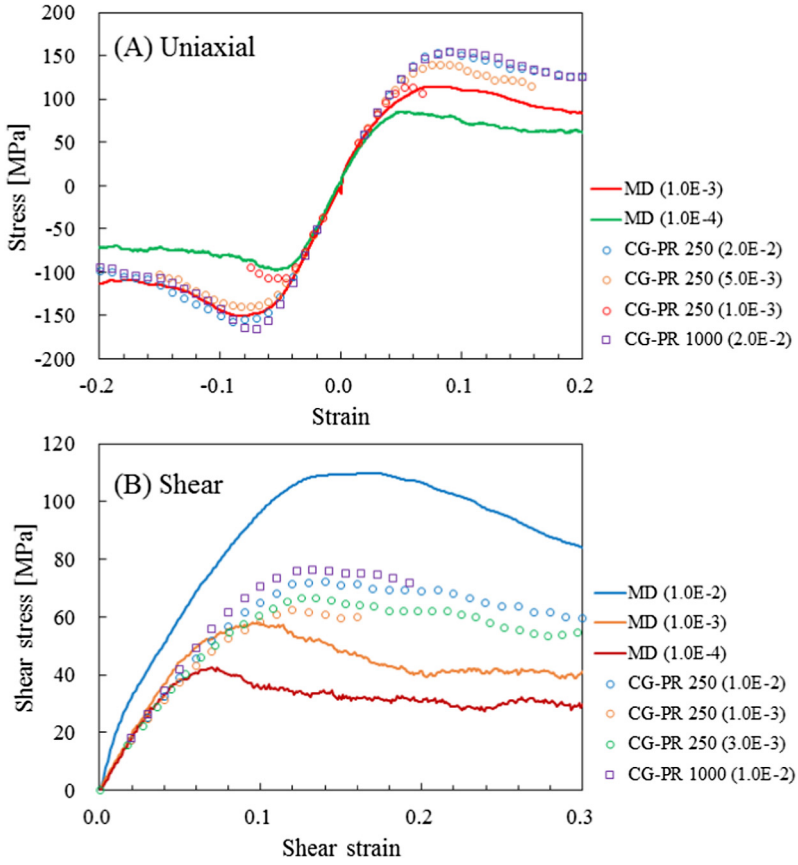

Fig. 10. Comparison of stress profile in uniaxial and shear deformations between MD (30,000 atoms) and CG-PR model with cubic specimen for Lennard-Jones binary glass.

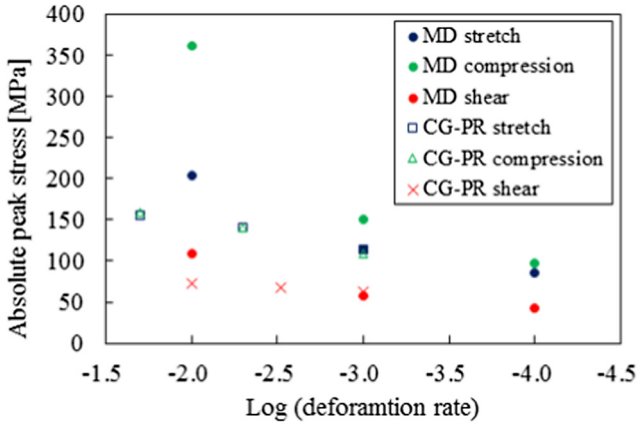

Fig. 11. Relation between deformation rate and stress peak for Lennard-Jones binary glass. MD model contains 30,000 atoms, and the CG-PR model is a cubic specimen with 100 elements.

$$\mathbf{B}^e := \left[\frac{\partial N^e}{\partial X}\right]. \tag{39}$$

The cohesive force vector $\mathbf{f}^{cohe}$ is the internal force contribution from the cohesive elements, or process zone elements. The cohesive force is controlled by the force-displacement relation of the atomic potential. Once the interactions among atoms inside the unit cell pass through the peak of the force-displacement relation in micro-scale, the cohesive force in the corresponding macroscale cohesive element will be also over the top of macroscale cohesive law, which is atomistically informed.

3. Numerical examples

3.1. Lennard-Jones binary glass

3.1.1. MD simulations

Firstly, we examined the effect of strain rate ($\dot{\varepsilon}$) on stress-strain (S-S) relation for the L-J binary glass by using MD simulations. We apply a suitable external stress to MD unit cell either elongating or compressing the unit cell in one direction (Z) with constant strain rate under periodic boundary conditions in any directions. The temperature was maintained at 0.01 in L-J unit to avoid thermal effect in attaining static yield stress.

Fig. 4A compares stress-strain curves of an 1000 atoms system with varying $\dot{\varepsilon}$ from 1.0×10^{-5} 1/s to 1.0×10^{-3} 1/s. Table 1 summaries the mechanical properties of the L-J binary glass. Elastic behavior can be recognized from −0.04 to 0.04 strain range, and the system subsequently shows ductile but not brittle fracture for all $\dot{\varepsilon}$. Young's modulus (E_y) estimated from the slope at the small strain remains within 15% deviation. On the other hand, both maximum and minimum stresses ($\sigma_{33}^{max}, \sigma_{33}^{min}$) depend on $\dot{\varepsilon}$, and a fast strain rate, say, 1.0×10^{-3} 1/s, will causes larger stress in both stretch and compression. Since the difference in strain rate between 1.0×10^{-4} 1/s and 1.0×10^{-5} 1/s is subtle, we deem that $\dot{\varepsilon} = 1.0\times10^{-4}$ 1/s is sufficiently slow to obtain static stress profile. At this strain rate, $\dot{\varepsilon} = 1.0\times10^{-4}$ 1/s, the overall stress-strain curve is analogous to any size of MD simulations. However, only 30,000 atoms MD system provides smooth the stress-strain relation, while smaller size MD systems always have oscillations in stress-strain relations due to the lack of statistics. Consequently,

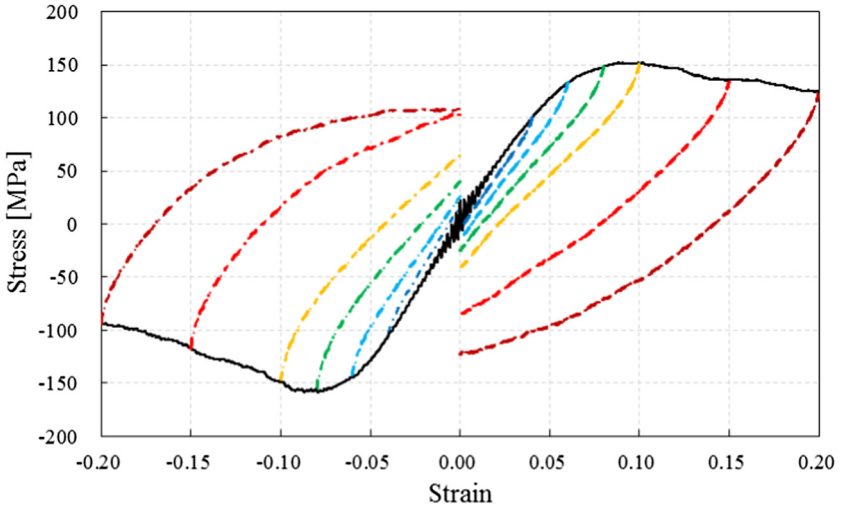

Fig. 12. Stress-strain hysteresis from both stretched and compressed conditions of Lennard-Jones binary glass with 250 atoms representative cell. Strain rate is ($\dot{\varepsilon} = 1.0 \times 10^{-2}$). Broken line is path from stretched shape and chain line is that from compressed shape.

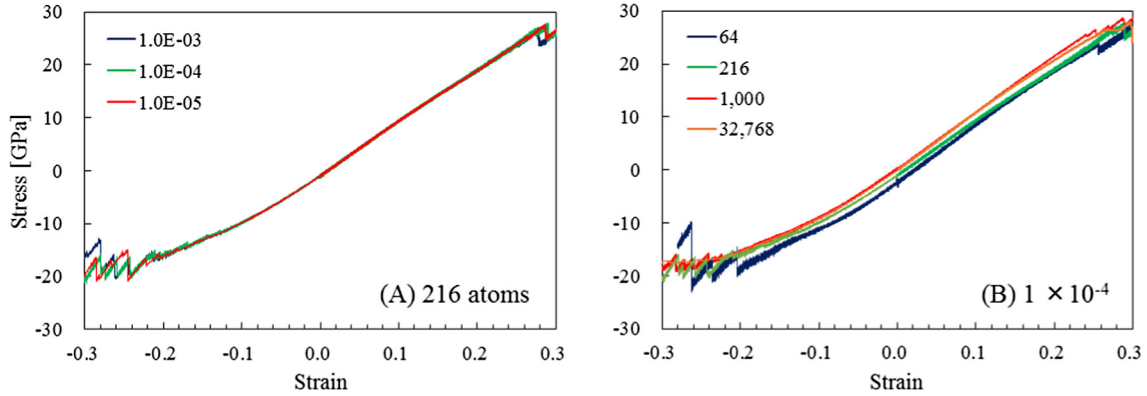

Fig. 13. MD simulation results of stress-strain relation of amorphous silicon. (A) 216 atoms system at $\dot{\varepsilon} = 1.0^{-3}$ to 1.0^{-5}. (B) 64, 216 and 1000 atoms systems at $\dot{\varepsilon} = 1.0^{-4}$, while 32,768 system at $\dot{\varepsilon} = 1.0^{-3}$.

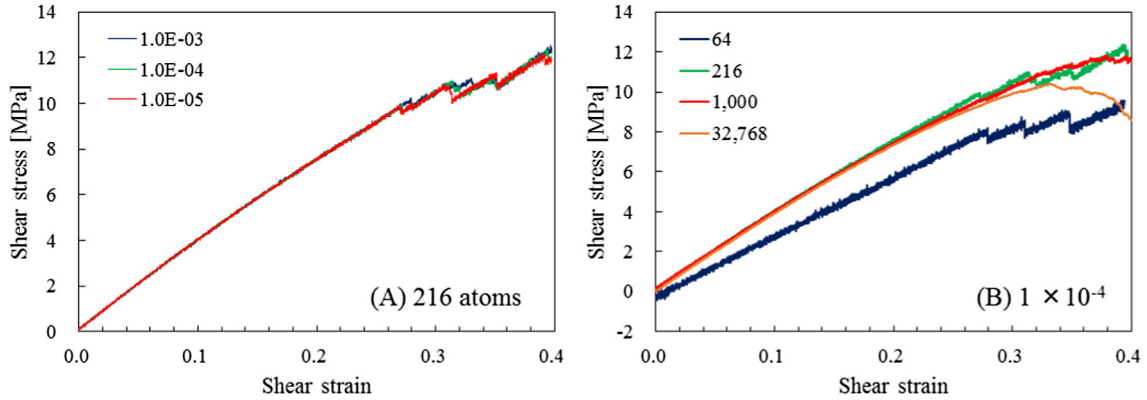

Fig. 14. MD simulation results of shear stress-strain relation of amorphous silicon. (A) 256 atoms system at $\dot{\gamma} = 1.0^{-3}$ to 1.0^{-5}. (B) 64, 256 and 1000 atoms systems at $\dot{\gamma} = 1.0^{-4}$, while 32,768 system at $\dot{\varepsilon} = 1.0^{-3}$.

smaller MD systems always show larger (absolute) value for both minimum and maximum stresses.

Next, shear stress (σ_{13}) was measured in the MD system that is being applied with constant shear strain rate ($\dot{\gamma}$). In this simulation, we divided the MD system into three domains. As seen in the schematic drawing in Fig. 5, atoms within 10% range of unit cell from both top and bottom are frozen. These two domains are treated as two parallel atomistic walls, then the atoms in upper wall slide to *X* direction at constant shear strain rate. Only those atoms in the body (middle) domain are allowed to relax according to the shear deformation generated by the confined domain. Periodic boundary conditions were applied in *X* and *Y* directions but not in *Z* direction, to which the three domains are in layered formation.

Table 2
Mechanical properties of amorphous silicon estimated by MD simulations.

No. of atom	Strain rate ($\dot{\varepsilon}$) shear rate ($\dot{\gamma}$)	E_y [GPa]	G [GPa]
64	1.0×10^{-4}	110	30.5
	1.0×10^{-3}	103	39.3
256	1.0×10^{-4}	101	39.3
	1.0×10^{-5}	103	39.4
1000	1.0×10^{-4}	107	38.5
32,768	1.0×10^{-3}	110	39.1

We have investigated the dependency of maximum stress and shear modulus (G) on shear strain rate for an 1000 atom MD system by using molecular dynamics, and the results obtained from the MD simulation is depicted in Fig. 6(A). At the range of 0.07–0.08 shear strain, the system reaches to the maximum shear stress. We found that the simulated shear modulus is insensitive to the shear strain rate; and the dependence of the maximum stress peak location (critical strain) on the shear strain rate is also relatively small. Vernik et al. has demonstrated that maximum shear stress of L-J binary glass highly depends on $\dot{\gamma}$ at $\overline{T} = 0.2$, while $\dot{\gamma}$ dependency is less at lower temperature [36]. Therefore, the very low temperature that we imposed in the MD simulation is the main reason why the shear stress is insensitive to shear strain rate.

On the one hand, the size effect on shear stress profile is apparent as shown in Fig. 6(B), and this is summarized in Table 1. Especially, the maximum stress is obviously higher at smaller system, implying that atom configurations are constrained more than that in the smaller unit cell.

3.1.2. Coarse-grained Parrinello-Rahman (CG-PR) method

To confirm the validity and reproducibility of CG-PR method, calculation condition of CG-PR method was investigated by using a simple FEM model composed of two bulk elements without CZ element, in which an r-cell containing multiple atoms is embedded in the center of the element (Fig. 7) or any quadrature points inside the element. Fig. 8 summarizes comparison between MD and CG-PR method for uniaxial and shear deformations with 250 atoms r-cell. Owing to careful tuning of CG parameters, it was possible to duplicate overall characteristics of S-S relations with even higher strain rate $\dot{\varepsilon}, \dot{\gamma} = 1.0 \times 10^{-2}$ 1/s, at which the MD simulation result shows larger maximum and minimum stresses. This might be due to the fact that CG-PR method can find local energy minimum in relatively wide range, while MD is more related to the time histories of atomic configuration and velocity. Note that atom configurations considered in MD and CG-PR method have much difference for shear deformation simulations, because the former did not account the atoms in boundary wall regions while undergoing shear deformation whereas the latter takes account all atoms in the r-cell.

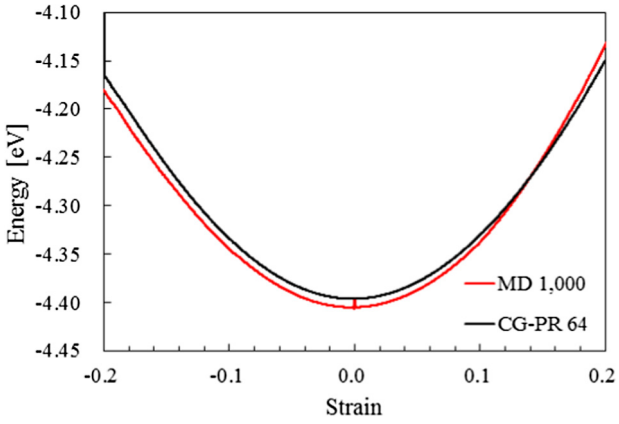

Fig. 16. Comparison of energy between CG-PR method and MD simulations by using cubic specimen. Energy of CG-PR method is average value of 100 elements.

After confirming that the CG-PR method works, we applied the method to a larger size continuum body, which is a cubic specimen composed of one hundred bulk elements without inserting CZ elements between the bulk elements. In this case, to make different amorphous microstructure, the r-cell was randomly rotated in each bulk element even though we only employ one generic microstructure for the r-cell. Fig. 9 shows the initial stress distribution of the cubic specimen with the arbitrarily rotated r-cells in different elements.

Comparison between the results obtained from both CG-PR method and MD are depicted in Fig. 10. In terms of uniaxial deformation, CG-PR method shows lower peaks of stress in both stretch and compression than MD simulations at the same strain rate. It indicates that the CG-PR method cannot represent fast deformation of amorphous materials even for zero-temperature condition, because CG-PR method finds more stable configurations than MD. In contrast, even though it was very time-consuming to conduct CG-PR simulation with strain rates ranging $\dot{\varepsilon} = 1.0 \times 10^{-4}$ 1/s, as the result demonstrated in the relation between the strain rate and peak stress shown in Fig. 11, we can conclude that CG-PR method is able to reproduce the stress-strain relation of MD simulations at the lower strain rate. Interestingly, there is no clear differences among the stress-strain relations measured under the strain rate $\dot{\gamma} = 2.0 \times 10^{-2}$ 1/s by increasing atoms in r-cell from 250 to 1000 atoms, even though the MD simulation result is size dependent.

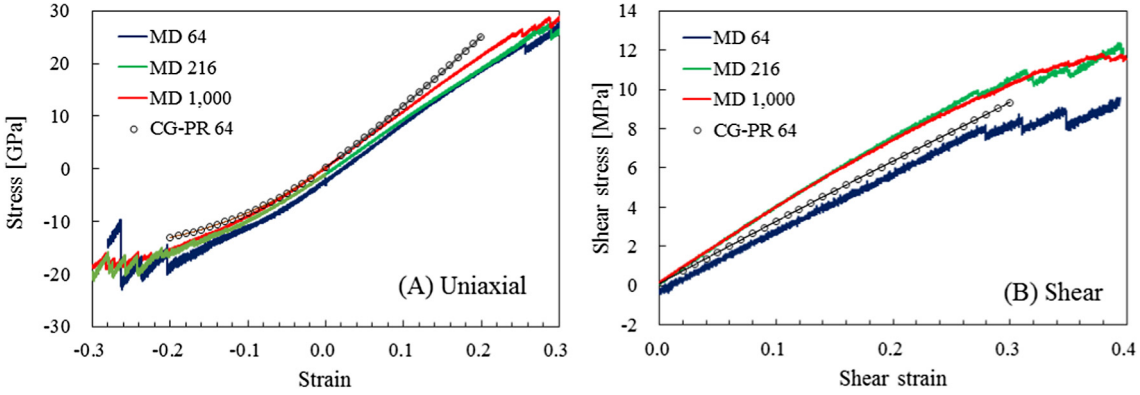

Fig. 15. Comparison of the results obtained by CG-PR method and MD simulations by using cubic specimen. (A) Uniaxial stretch and compression, (B) Shear deformation. $\dot{\varepsilon} = 1.0^{-4}$ and $\dot{\gamma} = 1.0^{-4}$ for MD. $\dot{\varepsilon} = 2.0^{-2}$ and $\dot{\gamma} = 1.0^{-2}$ for CG-BR.

For shear deformation, the simulation result of CG-PR method again shows lower peaks of stress at the same shear rate $\dot{\gamma}$ than that of MD simulation, even when the minimum r-cell is employed. Although it was difficult to simulate at $\dot{\gamma} = 1.0 \times 10^{-4}$ 1/s because of computation cost, one can expect that CG-PR method can reproduce the stress-strain relation at the strain rate reasonably, according to the results at higher deformation rate. On the other hand, there is no significant difference between them, even if we utilize larger r-cell with more than 1000 atoms.

In summary, even though the MD simulation of L-J binary glass shows system size dependency, especially for shear deformation, CG-PR method with minimum r-cell composed of 250 atoms can reasonably reproduce static stress-strain relation of the largest size of the MD system, when strain rate is slow enough. Moreover, CG-PR method may not have the unstable energy fluctuation phenomenon caused by high strain rate in MD simulations. This is because that CG-PR computation is more stable than that of MD computation. This is due to the fact that the proposed CG-PR is still a zero-temperature calculation, and it is a macroscale calculation with much larger size.

In order to capture that plastic deformation in the multiscale simulation, we applied the same strain rate ($\dot{\varepsilon} = 1.0 \times 10^{-2}$ 1/s) from tension to compression at the strain range 0.04–0.2 to the cubic specimen. We recorded the loading-uploading stress-strain relation in Fig. 12. As shown in Fig. 12, the measured stress-strain relation shows hysteresis characteristics, indicating that the proposed multiscale method is able to capture plastic deformation and history dependent behaviors based on the atomistic mechanism and information. To the best of the authors' knowledge, this is the first successful multiscale simulation or realization of plastic deformation at mesoscale or macroscale without using molecular dynamics or empirical plasticity theories. The reason for such success is because that we optimized atom configurations in the r-cell, and it makes the atom configuration irreversible, which reflects and captures the irreversible nature of plastic deformations.

3.2. Amorphous silicon (a-Si solid)

3.2.1. MD simulations

We first carried out a series of MD simulations of a-Si solid to examine the effects of strain rate ($\dot{\varepsilon}$) and shear rate ($\dot{\gamma}$) on the mechanical responses of a-Si solid to the deformation. The simulation procedure is almost the same with L-J binary glass except for temperature, which was maintained at 10 [K] during the simulations. As demonstrated in Fig. 13(A), in contrast to the L-J binary glass, there is no clear difference in stress-strain curve for uniaxial deformation among all system sizes from 64 to 32,768 atoms. In addition, the a-Si system is insensitive to $\dot{\varepsilon}$ in both stretch and compression tests (see Fig. 13(B)). Therefore even the smallest size system of 64 atoms can reproduce E_y with reasonable accuracy. In terms of shear deformation, Fig. 14(A) shows that 64 atoms system slightly underestimates shear modulus, but 216 atoms system is almost identical to 1000 atoms representative cell. For the 216 atoms r-cell, shear modulus is nearly unchanged with the strain rate $\dot{\gamma}$ (Fig. 14(B)). E_y and G obtained in small deformation range are tabulated in Table 2. Both of these elastic constants are 12–19% and 29–40% smaller than the experimental values reported in the literature, e.g. $E_y = 125 \pm 1$ [GPa] [51] and $G = 55.7$ [GPa] [52,53], respectively.

It is noted that the yield stress obtained from MD simulations is exceedingly higher than that obtained from experimental observations (e.g. 6.1 ± 0.8 [GPa] [54], 6.9 [GPa] [55] for single-crystal silicon, and 4.94 ± 0.93 [GPa] for a-Si [53]). This is because the well known drawback of classical three body potentials including the Tersoff potential [56,57], one has to keep in mind that any MD and CG-PR simulations with the Tersoff potential are only suitable for elastic responses, but not for damage processes, such as dislocation, bond breakage, cavity nucleation, and fracture.

3.2.2. CG-PR method

We have applied the CG-PR method to study mechanical properties of a-Si solid by using the cubic specimen that is the same as that of the L-J binary glass. The CG-PR method referred here is a multiscale finite element method, in which the constitutive equations of amorphous materials are obtained from atomistic potential. In CG-PR method, during constitutive update, we first use the Cauchy-Born rule to guess the deformed configuration of the amorphous solid, and then use static molecular mechanics, i.e. CG-PR method to find the optimized configuration of the amorphous solid. Here, we only use CG-PR method to simulate elastic properties of amorphous materials, and therefore we treat all the finite elements as the regular bulk elements, meaning that there is no cohesive elements involved. The plastic deformation and material damage will be discussed later in the multiscale cohesive zone model (MCZM).

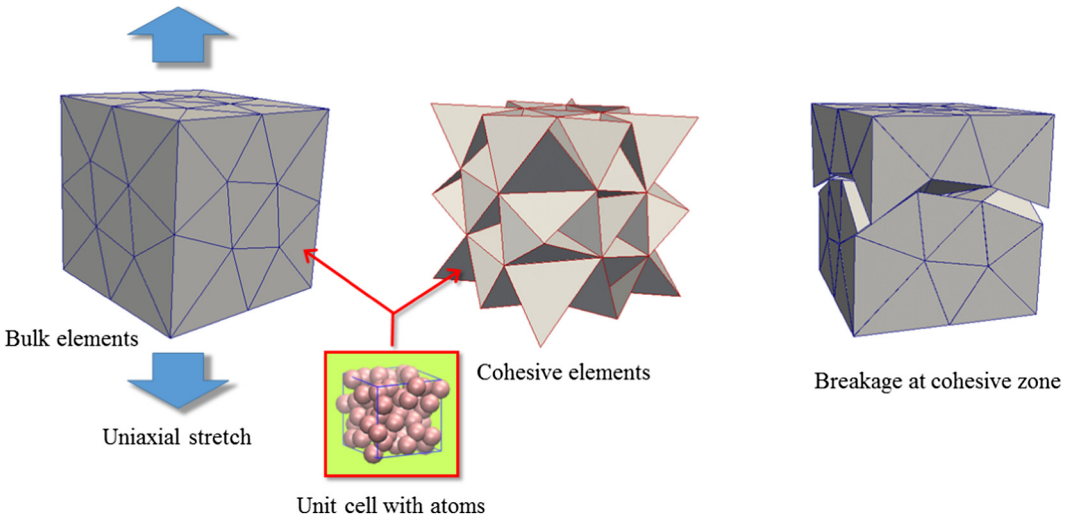

Fig. 17. Benchmark MCZM simulation of fracture in amorphous materials.

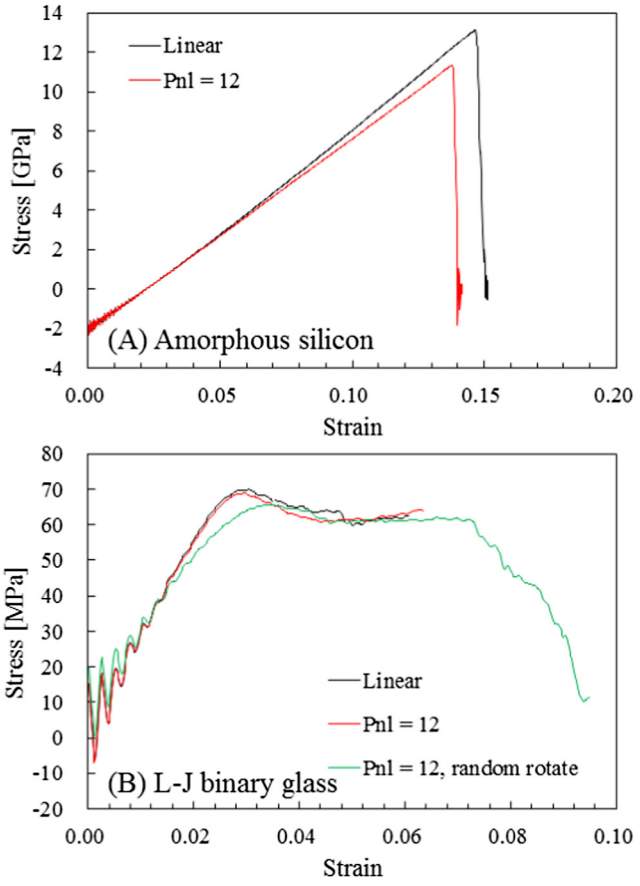

Fig. 18. Strain-stress relation and fracture stress of (A) amorphous silicon and (B) Lennard-Jones binary glass.

The simulation setting for CG-PR method, such as periodic boundary condition and loading strain rates, are the same for both a-Si solid and L-J binary glass. The smallest r-cell that contains 64 atoms is used in the simulation, because we found that there is no clear size dependence in MD simulations. As shown in Fig. 15, the stress-strain relations obtained by using CG-PR method are close enough to those obtained by MD simulations with 1000 atoms for both uniaxial and shear deformations, although deviation from MD result becomes larger as strain increases in the case of uniaxial stretch. Fig. 16 compares energy profiles for the case of uniaxial deformation, and we have found that average energy over all elements in CG-PR method is lower than the average energy in MD model when $\varepsilon > 0.15$. This result implies that CG-PR method can appropriately find local energy minimum, and as a coarse-grain method CG-PR provides good accuracy in prediction of average energy. Therefore, we conclude that for a-Si solids it is possible to use small size of r-cell to reproduce larger scale MD simulation results by using CG-PR method in combination with CBR, even when strain rates are relatively large. This is remarkably different from the case of L-J binary glass. However, in both cases, we can use the minimum or smallest r-cell to reasonably estimate mechanical properties of the material by using CG-PR method with CBR under moderate strain rate conditions.

4. MCZM simulations of fracture in amorphous materials

In this section, we discuss the implementation of CG-PR method with the Multiscale Cohesive Zone Method (MCZM) to simulate plastic deformation and fracture of the amorphous materials. The main idea of the Multiscale Cohesive Zone Model (MCZM) is to insert thin a CZ element between bulk elements such that one can simulate fracture of amorphous materials automatically. The specimen used in MCZM simulations is almost the same as shown in Fig. 9, however, additional 158 CZ elements are inserted between the bulk elements to represent fracture process zone. Amorphous r-cells are also embedded into these CZ elements (Fig. 17). The size of the minimum r-cells that are employed in the simulation has 250 atoms for L-J binary glass and 64 atoms for a-Si solid, respectively. This is because we have confirmed that they can be reasonably applied to simulate mechanical properties in comparison with large scale MD simulations. In the numerical simulation, we applied uniaxial stretch in Z-direction and measured stress-strain relation. Fig. 18 displays the stress-strain curves for both of L-J binary glass and a-Si solid.

In the case of a-Si solid, one can clearly observe brittle fracture and sharp stress drop after yield stress. The yield stress is about 13 [GPa] if only linear deformation is considered in CZ element, and the stress is decreased if we take inhomogeneous deformation into account with parameter $P_{nl} = 12$. As discussed in our previous work, which has studied fracture of single-crystal silicon [6], here we can again confirm that nonuniform deformation provokes weakness of CZ element even for amorphous configuration. Note that the estimated yield stress is somewhat larger than experiment [53], even though experimental measurement data on the yield stress of a-Si is very limited. Since our specimen would be too rough to discuss quantitatively, we should utilize more precise model to judge the accuracy.

On the other hand, a long plateau can be seen in the stress-strain relation for L-J binary glass after the stress reaches to yield stress. This occurs at relatively small deformation $\varepsilon = 0.03$. After that, the specimen fractures at $\varepsilon = 0.07$. This result is reasonable, because L-J binary glass with the parameter set that we adopted is known to have ductile behavior [31,32,36]. To the best of authors' knowledge, this study might provide the first demonstration of ductile fracture by using CBR-based method combined with CZ model. The multiscale method developed here may be also applied to simulate fracture of metallic materials as well as other types of ductile materials that are governed by ductile failure mechanism, with the insight of atomistic modeling.

5. Conclusions

In this work, we have studied the possibility as well as applicability to use the Cauchy-Born rule based multiscale methods to model amorphous materials. In particular, we have applied two CBR based multiscale methods, i.e. the coarse-grained Parrinello-Rhman (CG-PR) method and the multiscale cohesive zone method (MCZM) studying two amorphous materials, i.e. Lennard-Jones binary glass and amorphous silicon (a-Si). By using r-cells with different sizes constructed by using MD, the results obtained by CG-PR method are comparable with large scale MD simulations. The results of the both molecular dynamics and multiscale simulation show that the two amorphous materials have different behaviors.

In MD simulations, L-J binary glass demonstrates system size dependence of stress-strain relations in uniaxial tension, compression and also shear deformation tests. Because strain rate significantly affects peak value of the stress, sufficiently slow deformation rate is necessary in order to estimate static stress-strain relation during MD simulations. In contrast, CG-PR method can reach to more stable condition even at high strain rates, the peak stress is lower than that of MD at higher strain rates. Therefore, the results obtained by using CG-PR method agrees with that of MD simulation only when strain rate is small enough. Interestingly, the results obtained by using the minimum r-cell with 250 atoms agrees with that of a larger scale MD with 30,000 atoms in

stress peak value, while there is no sufficient improvement by increasing atom number in the r-cell up to 1000 atoms.

Stress profile of a-Si was almost identical in any unit cell sizes and also deformation rates. Therefore, it was possible to reproduce S-S curves of uniaxial stretch, compression and shear deformation, by using the minimum r-cell with only 64 atoms even with relatively fast deformation rate.

According to these results, we can conclude that CBR is applicable even for amorphous materials at quasi-static condition with slow deformation, despite the fact that the rule basically assumes uniform deformation. Although adequate number of atoms in r-cell should be maintained for each material, two typical amorphous materials studied in this work require only minimum size of the r-cell whose side length is about twice of cutoff distance of the interatomic potential.

After a preliminary study, we have simulated the fracture and damage of cubic specimens of both L-J binary glass and a-Si solid by using the Multiscale Cohesive Zone Model, in which we employ an extremely thin element between bulk elements for the fracture process zone. As a result, a-Si solid clearly showed brittle fracture pattern, although the number of elements of the model is not large enough to make an accuracy prediction or quantitative prediction. It was also confirmed in our study that the process zone elements in MCZM can produce incipient fracture condition or crack formation if the higher order nonlinear deformation in CZ element is imposed as discussed in our previous work [6]. On the other hand, the simulation results on L-J binary glass show features of ductile fracture, which in consistent with MD simulations of the system e.g. [31,32,36]. It indicates that we can simulate ductile fracture in amorphous metals, polymers, adhesive materials and also grain boundaries of polycrystalline metals by using CG-PR method with using amorphous r-cells. In summary, we have shown in this work that the CBR procedure is applicable for amorphous materials as a first-order approximation to estimate constitutive relation based on atom configurations in continuum domain. The special CBR technique presented in this paper allows us to extend multiscale modeling to a host of non-crystal amorphous materials.

Acknowledgements

The authors would like to thank the editor and reviewer's suggestion on simulation of plastic deformation of amorphous materials.

Dr. S. Urata is sponsored by Asahi Glass Co., Ltd. Japan, and this support is greatly appreciated.

References

[1] J. Ericksen, On the cauchy-born rule, Math. Mech. Solids 13 (3–4) (2008) 199–220.
[2] R.E. Miller, E.B. Tadmor, The quasicontinuum method: overview, applications and current directions, J. Comput. Aided Mater. Des. 9 (3) (2002) 203–239.
[3] H. Gao, B. Ji, Modeling fracture in nanomaterials via a virtual internal bond method, Eng. Fract. Mech. 70 (2003) 1777–1791.
[4] X. Zeng, S. Li, A multiscale cohesive zone model and simulations of fractures, Comput. Methods Appl. Mech. Eng. 199 (9) (2010) 547–556.
[5] E.B. Tadmor, M. Ortiz, R. Phillips, Quasicontinuum analysis of defects in solids, Phil. Mag. A 73 (6) (1996) 1529–1563.
[6] S. Urata, S. Li, Higher order cauchy-born rule based multiscale cohesive zone model and prediction of fracture toughness of silicon thin films, Int. J. Fract. 23 (1) (2017) 159–181.
[7] E. Tadmor, G. Smith, N. Bernstein, E. Kaxiras, Mixed finite element and atomistic formulation for complex crystals, Phys. Rev. B 59 (1) (1999) 235.
[8] L. Xiong, Q. Deng, G.J. Tucker, D.L. McDowell, Y. Chen, Coarse-grained atomistic simulations of dislocations in al, ni and cu crystals, Int. J. Plast. 38 (2012) 86–101.
[9] A. Ramasubramaniam, E.A. Carter, Coupled quantum–atomistic and quantum–continuum mechanics methods in materials research, MRS Bull. 32 (11) (2007) 913–918.
[10] R. Sunyk, P. Steinmann, On higher gradients in continuum-atomistic modelling, Int. J. Solids Struct. 40 (24) (2003) 6877–6896.
[11] J.Z. Yang, E. Weinan, Generalized cauchy-born rules for elastic deformation of sheets, plates, and rods: derivation of continuum models from atomistic models, Phys. Rev. B 74 (18) (2006) 184110.
[12] M. Arroyo, T. Belytschko, Finite crystal elasticity of carbon nanotubes based on the exponential cauchy-born rule, Phys. Rev. B 69 (11) (2004) 115415.
[13] H.S. Park, P.A. Klein, G.J. Wagner, A surface cauchy-born model for nanoscale materials, Int. J. Numer. Methods Eng. 68 (10) (2006) 1072–1095.
[14] H.S. Park, P.A. Klein, A surface cauchy-born model for silicon nanostructures, Comput. Methods Appl. Mech. Eng. 197 (41) (2008) 3249–3260.
[15] A. Khoei, H. DorMohammadi, A. Aramoon, A temperature-related boundary cauchy–born method for multi-scale modeling of silicon nano-structures, Phys. Lett. A 378 (5) (2014) 551–560.
[16] S. Li, B. Ren, H. Minaki, Multiscale crystal defect dynamics: a dual-lattice process zone model, Phil. Mag. 94 (13) (2014) 1414–1450.
[17] S. Alexander, Amorphous solids: their structure, lattice dynamics and elasticity, Phys. Rep. 296 (2) (1998) 65–236.
[18] S. Li, G. Wang, Introduction to Micromechanics and Nanomechanics, World Scientific Pub., Singapore, 2008.
[19] J.D. Eshelby, The determination of the elastic field of an ellipsoidal inclusion and related problems, Proc. Roy. Soc. London A: Math. Phys. Eng. Sci., vol. 241, The Royal Society, 1957, pp. 376–396.
[20] H. Liu, L. Sun, Multi-scale modeling of elastoplastic deformation and strengthening mechanisms in aluminum-based amorphous nanocomposites, Acta Mater. 53 (9) (2005) 2693–2701.
[21] T. Albaret, A. Tanguy, F. Boioli, D. Rodney, Mapping between atomistic simulations and eshelby inclusions in the shear deformation of an amorphous silicon model, Phys. Rev. E 93 (5) (2016) 053002.
[22] P. Valavala, T. Clancy, G. Odegard, T. Gates, E. Aifantis, Multiscale modeling of polymer materials using a statistics-based micromechanics approach, Acta Mater. 57 (2) (2009) 525–532.
[23] V. Tan, X. Zeng, M. Deng, K. Lim, T. Tay, Multiscale modeling of polymers–the pseudo amorphous cell, Comput. Methods Appl. Mech. Eng. 197 (6) (2008) 536–554.
[24] Z.C. Su, T.-E. Tay, Y. Chen, V.B. Tan, Multiscale modeling for amorphous materialsmapping atomistic displacements to macroscopic deformation, Int. J. Appl. Mech. 4 (04) (2012) 1250037.
[25] Z. Su, V. Tan, T. Tay, Concurrent multiscale modeling of amorphous materials in 3d, Int. J. Numer. Methods Eng. 92 (13) (2012) 1081–1099.
[26] M.C. Araújo, J. Martins, S. Mirkhalaf, S. Lanceros-Mendez, F.A. Pires, R. Simoes, Predicting the mechanical behavior of amorphous polymeric materials under strain through multi-scale simulation, Appl. Surf. Sci. 306 (2014) 37–46.
[27] Y. Davit, J. Osborne, H. Byrne, D. Gavaghan, J. Pitt-Francis, Validity of the cauchy-born rule applied to discrete cellular-scale models of biological tissues, Phys. Rev. E 87 (4) (2013) 042724.
[28] B. Rech, H. Wagner, Potential of amorphous silicon for solar cells, Appl. Phys. A 69 (2) (1999) 155–167.
[29] L. Han, K. Song, P. Mandlik, S. Wagner, Ultraflexible amorphous silicon transistors made with a resilient insulator, Appl. Phys. Lett. 96 (4) (2010) 042111.
[30] W. Kob, H.C. Andersen, Testing mode-coupling theory for a supercooled binary Lennard-Jones mixture I: The van hove correlation function, Phys. Rev. E 51 (5) (1995) 4626.
[31] M. Falk, Molecular-dynamics study of ductile and brittle fracture in model noncrystalline solids, Phys. Rev. B 60 (10) (1999) 7062.
[32] C.D. Lorenz, M.J. Stevens, Fracture behavior of Lennard-Jones glasses, Phys. Rev. E 68 (2) (2003) 021802.
[33] S. Plimpton, Fast parallel algorithms for short-range molecular dynamics, J. Comput. Phys. 117 (1) (1995) 1–19.
[34] J. Tersoff, Empirical interatomic potential for silicon with improved elastic properties, Phys. Rev. B 38 (14) (1988) 9902.
[35] J. Tersoff, Modeling solid-state chemistry: interatomic potentials for multicomponent systems, Phys. Rev. B 39 (8) (1989) 5566.
[36] F. Varnik, L. Bocquet, J.-L. Barrat, A study of the static yield stress in a binary Lennard-Jones glass, J. Chem. Phys. 120 (6) (2004) 2788–2801.
[37] A. Raghunathan, J. Park, N. Aluru, Interatomic potential-based semiclassical theory for Lennard-Jones fluids, J. Chem. Phys. 127 (17) (2007) 174701.
[38] M. Ishimaru, S. Munetoh, T. Motooka, Generation of amorphous silicon structures by rapid quenching: a molecular-dynamics study, Phys. Rev. B 56 (23) (1997) 15133.
[39] E.B. Tadmor, R.E. Miller, Modeling Materials: Continuum, Atomistic and Multiscale Techniques, Cambridge University Press, 2011.
[40] S. Nosé, A unified formulation of the constant temperature molecular dynamics methods, J. Chem. Phys. 81 (1) (1984) 511–519.
[41] M. Parrinello, A. Rahman, Polymorphic transitions in single crystals: a new molecular dynamics method, J. Appl. Phys. 52 (12) (1981) 7182–7190.
[42] S. Li, S. Urata, An atomistic-to-continuum molecular dynamics: theory, algorithm, and applications, Comput. Methods Appl. Mech. Eng. 306 (2016) 452–478.
[43] P. Podio-Guidugli, On (andersen)-parrinello-rahman molecular dynamics, the related metadynamics, and the use of the cauchy-born rule, J. Elast. 100 (2010) 145–153.
[44] S. Li, Q. Tong, A concurrent multiscale micromorphic molecular dynamics, J. Appl. Phys. 117 (2015) 54303, http://dx.doi.org/10.1063/1.4916702.

[45] X. Xu, A. Needleman, Numerical simulation of fast crack growth in brittle solids, J. Mech. Phys. Solids 42 (1994) 1397–1434.
[46] K.Y. Volokh, Comparison between cohesive zone models, Commun. Numer. Methods Eng. 20 (11) (2004) 845–856.
[47] D. Lyu, H. Fan, S. Li, A hierarchical multiscale cohesive zone model and simulation of dynamic fracture in metals, Eng. Fract. Mech. 163 (2016) 327–347.
[48] M. He, S. Li, An embedded atom hyperelastic constitutive model and multiscale cohesive finite element method, Comput. Mech. 49 (3) (2012) 337–355.
[49] J. Qian, S. Li, Application of multiscale cohesive zone model to simulate fracture in polycrystalline solids, J. Eng. Mater. Technol. 133 (1) (2011) 011010.
[50] L. Liu, S. Li, A finite temperature multiscale interphase zone model and simulations of fracture, J. Eng. Mater. Technol. 134 (3) (2012) 031014.
[51] M. Szabadi, P. Hess, A. Kellock, H. Coufal, J. Baglin, Elastic and mechanical properties of ion-implanted silicon determined by surface-acoustic-wave spectrometry, Phys. Rev. B 58 (14) (1998) 8941.
[52] P. Burnett, G. Briggs, The elastic properties of ion-implanted silicon, J. Mater. Sci. 21 (5) (1986) 1828–1836.
[53] D.M. Follstaedt, J. Knapp, S. Myers, Mechanical properties of ion-implanted amorphous silicon, J. Mater. Res. 19 (01) (2004) 338–346.
[54] F. Ericson, J.-Å. Schweitz, Micromechanical fracture strength of silicon, J. Appl. Phys. 68 (11) (1990) 5840–5844.
[55] K.E. Petersen, Silicon as a mechanical material, Proc. IEEE 70 (5) (1982) 420–457.
[56] K. Kang, W. Cai, Brittle and ductile fracture of semiconductor nanowires–molecular dynamics simulations, Phil. Mag. 87 (14–15) (2007) 2169–2189.
[57] J.A. Hauch, D. Holland, M. Marder, H.L. Swinney, Dynamic fracture in single crystal silicon, Phys. Rev. Lett. 82 (19) (1999) 3823.